Quantitative data analysis and multiparameter inversion of Biot wave data: insights from topology and geometry

James Wiskin,[a] John Klock[a]
[a]QT Imaging, Inc., Novato, USA

Abstract

Evidence for Biot slow wave data in 3D ultrasound tomographic (3D UT) data from an orthopedic scan is shown by segmentation interior to Bone. Previous results have shown the quantitative accuracy of the 3D ultrasound volography method for ligaments, cartilage, tendons, skin, fat, muscle, etc.

Interior to bone the SOS values are lower than expected. It is known that a slow compressional wave is predicted by Johnson-Biot theory which has speed of sound (SOS) values independently measured which are similar to our values based on segmentation for trabecular bone matrix interior to bone. Values for marrow are determined from segmentation and are commensurate with literature values as well.

Concepts from algebraic topology are applied to the tomographic data (the first homotopy group of the N-torus, where N is the number of receiver elements in the array) and a quantitative comparison of the data redundancy with 2D algorithms is carried out. The use of algebraic topology gives a suitable context in which to understand phase unwrapping issues and leads to constraints on the distance between the data acquisition (DA) data levels and the frequencies used in the reconstruction.

The data redundancy comparison applies to any 3D vs 2D comparison, e.g. 3D UT compared with MRI and shows the much larger size of the information contributing to a single voxel in the 3D vs 2D as long as the 3D model for wave propagation is used. The implications of this are discussed.

Validation of attenuation variation with frequency is shown.

Key Words

3D ultrasound tomography, Biot slow wave, quantitative ultrasound, porous media, data analysis, orthopedic imaging, osteoporosis, data topology

Introduction

Low frequency 3D ultrasound tomography has established itself as a bona fide imaging modality in breast [1, 2], orthopedic, and pediatric scenarios. The breast scanner for QT Imaging, Inc. is FDA cleared for diagnostic purposes and is deployed presently in several clinics domestically and internationally, with more slated for the near future. The algorithm itself has been tested in a prototype scenario for the knee (orthopedics) and a whole pig has been imaged [3, 4]. There are in fact two distinct modalities: 1. The speed of sound (SOS) and attenuation (ATTEN) and 2. refraction corrected reflection image.

The first are obtained via the model based transmission algorithm, and the second by utilizing ray tracing through inhomogeneous media These are strictly proof of concept (POC) scans but do show the remarkable capability of the algorithm to give high resolution (~1 mm FWHM, and sub mm detectability) in refraction corrected reflection images even in the presence of bone and air.

Initial results have also been obtained from ex-vivo prostates, where the clinical observability of the prostate cancer was compared favorably with MRI[5-7]. This was also POC, however, the initial results above with bone and air indicate the possibility of in vivo imaging.

Note also that the bone in the femur and tibia is trabecular and thus is a matrix of bone structure that is filled with marrow. This is ideal for modelling with the Biot wave theory of wave propagation[8]. The existence of the slow compressional wave characteristic of Biot wave theory has been independently verified[9-12]. We desire to show the reconstruction of a cadaver knee with previously verified quantitative speed of sound (SOS) and extend this to show the wave speed interior to the bone is commensurate with the slow compressional

Medical Imaging 2024: Ultrasonic Imaging and Tomography, edited by Christian Boehm, Nick Bottenus,
Proc. of SPIE Vol. 12932, 129321B · © 2024 SPIE · 1605-7422
doi: 10.1117/12.3006543

wave predicted by Biot wave theory. Kramers-Kronig relations and measured data have shown the frequency dependence of the true wavenumber, which we show experimentally[13].

We discuss specific phase unwrapping phenomena that are understood in terms of concepts from algebraic topology (first and second homotopy groups of a manifold.[14]). Although not necessary, these concepts are the natural arena to discuss these phenomena in a comprehensive manner.[15]

Images are displayed of relevant reconstructions of speed of sound and segmentations.

Figure 1: QT Imaging scanner, showing water bath in which, the cadaver knee was placed and scanned.

Methods

Segmentation is constrained by a 3D ellipsoid on SOS images from the QT Imaging scanner adapted for the cadaver knee with a holder to hold the knee upright in the water bath[4]. Segmentation of the marrow region and the trabecular bone are carried out independently based on speed of sound values[14].

The data are collected on a 256 by 8 row array rotating 360 degrees around the leg, then moving up 2 mm and the array rotating in the opposite direction and repeating until the entire leg is scanned. This data acquisition (DA) process can be signified by $(\theta,l)\in S^1\times R$ giving position of the array, and the map:

$(\theta,l)\to(\theta_1,\cdots,\theta_N,r_1,\cdots,r_N)$, where $r_j e^{i\theta_j}$ is the complex signal received at receiver *j*, $1\le j\le N=8\times 256$ for a given frequency. This is interpreted as a map between manifolds, in particular:

$$g:(\theta,l)\in S^1\times R^1\to(\theta_1,\cdots,\theta_N,r_1,\cdots,r_N)\in T^N\times R^N\approx T(T^N) \tag{1}$$

(see below). Here we use the fact that the tangent bundle to the *N-torus* is trivial[14] for the identification of $T^N\times R^N\approx T(T^N)$, . Also the explicit identification of $(r_1,\cdots,r_N)\in R^N\approx T_\Theta(T^N)$, where $T_\Theta(T^N)$ is the tangent plane at $\Theta\equiv(\theta_1,\cdots,\theta_N)\in T^N$, the N-torus, is given below.

The reconstruction algorithm produces a speed of sound (SOS) and attenuation image (ATTEN) from this map between manifolds.

The segmented values for the trabecular bone is taken at several locations in the femur and the tibia and compared with literature values for bone. The marrow is also segmented in several places and statistics gathered.

For breast and soft tissue the variable density may perhaps be ignored, but for orthopedic applications density should be accounted for. In the past this has been accomplished via the simultaneous inversion of two parameters, density and speed of sound. However, the inversion of density is ill-posed due to its dipole scattering . The case for variable density could be obtained by transforming the Helmholtz equation with variable density via $g(\mathbf{x})\equiv f(\mathbf{x})/\sqrt{\rho}$, where ρ is the mass density and isolating the frequency independent k_o part of resulting pseudo-wave number $k'^2(\mathbf{x})\equiv k_f^2+k_0^2$, which then allows the determination of the density.

Thus, the variation of attenuation and SOS with frequency (the spectrum) is required. These are measured phenomenologically (see below).

Johnson-Biot Theory:

$$\begin{pmatrix} \hat{\rho}_{11} & \hat{\rho}_{12} \\ \hat{\rho}_{21} & \hat{\rho}_{22} \end{pmatrix} \begin{pmatrix} \partial_t^2 \mathbf{u} \\ \partial_t^2 \mathbf{U} \end{pmatrix} = \begin{pmatrix} P & Q \\ Q & R \end{pmatrix} \begin{pmatrix} \nabla(\nabla.\mathbf{u}) \\ \nabla(\nabla.\mathbf{U}) \end{pmatrix} - \begin{pmatrix} N(\nabla \times \nabla \times \mathbf{u}) \\ 0 \end{pmatrix} \quad (2)$$

The coefficients $\hat{\rho}_{ij}$, *N, Q, R, and P* relate to mass density of fluid, dynamic tortuosity, permeability and viscous characteristic length and arise out of the contribution of Johnson et al.[2] and Biot's original paper[16-21]. This theory predicts a 'slow' compressional wave: SOS =~1470 m/s (temperature and frequency dependent), which is slower than the standard compressional wave[10].

Results

Biot wave reconstruction

Below we show the segmentation of trabecular bone for femur in all 3 views. The SOS of the segmented region is shown to be approximately equal to the literature value for the Biot slow wave.

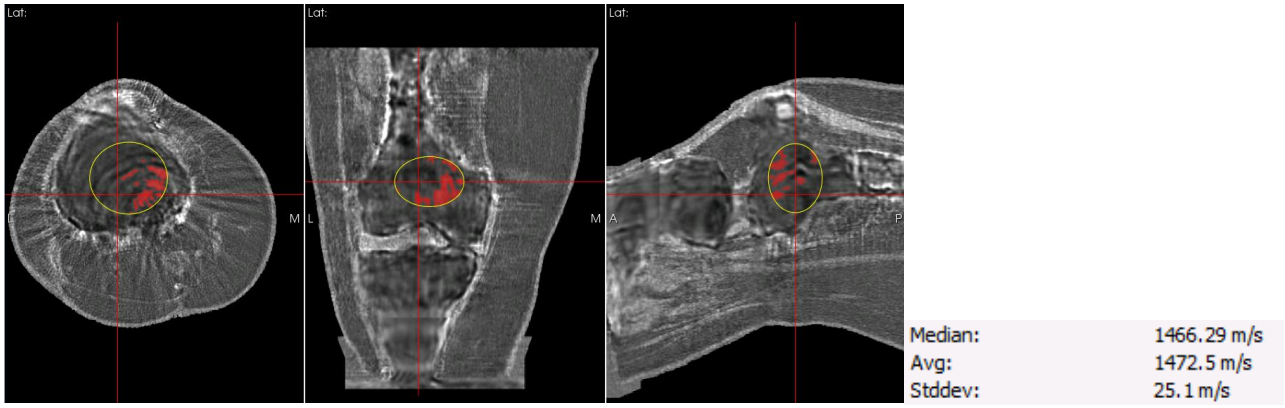

Figure 2: Left: axial, coronal, sagittal images of cadaver knee showing segmentation of trabecular bone and concomitant statistics. The speed of sound interior to trabecular bone is seen to be lower than expected but is very close to literature values for the Johnson-Biot slow wave.(1470 m/s). See below.

Below are segmentations of the speed of sound for tibia. The left panel shows segmentation of the marrow and the resulting speed of sound estimate is 1389 m/s

Table 1

	Literature values	*QTUS measured values*
Marrow	*~1410 m/s*	*1402, 1389 m/s*
Biot slow P wave	*~1470 m/s [2, 3]*	*1472, 1466 m/s*

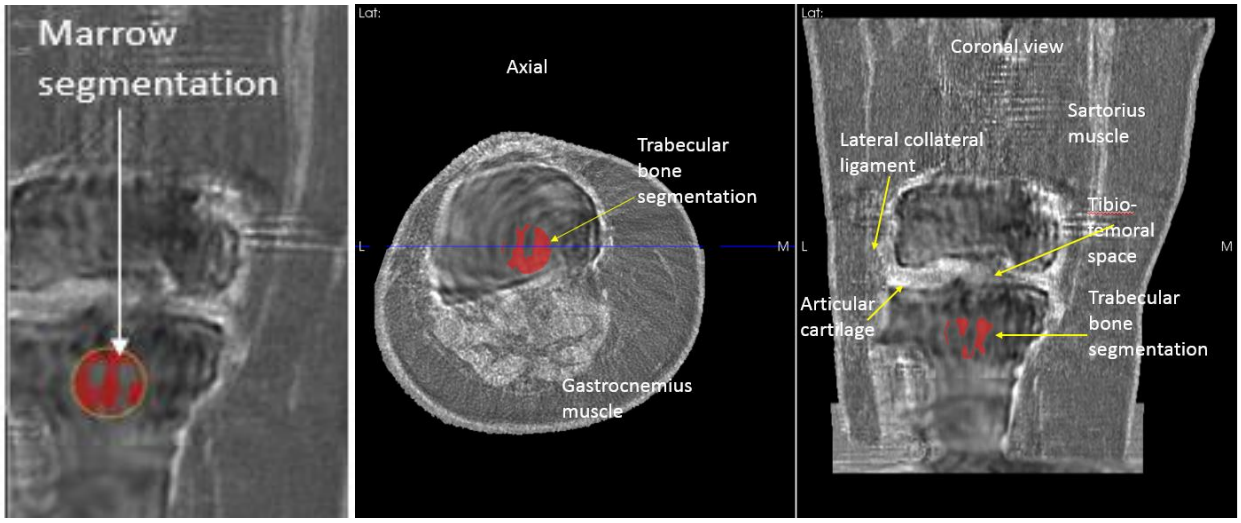

Figure 3 Left to right: Coronal view, with marrow segmentation shown in red. Axial and coronal view of cadaver knee 3D ultrasound speed of sound image (SOS) with bone segmented region shown in red. This has an average SOS = 1466 m/s (SD = 29.9) which agrees with estimates of slow P wave SOS in human femur at 0.4 – 0.8 MHz.

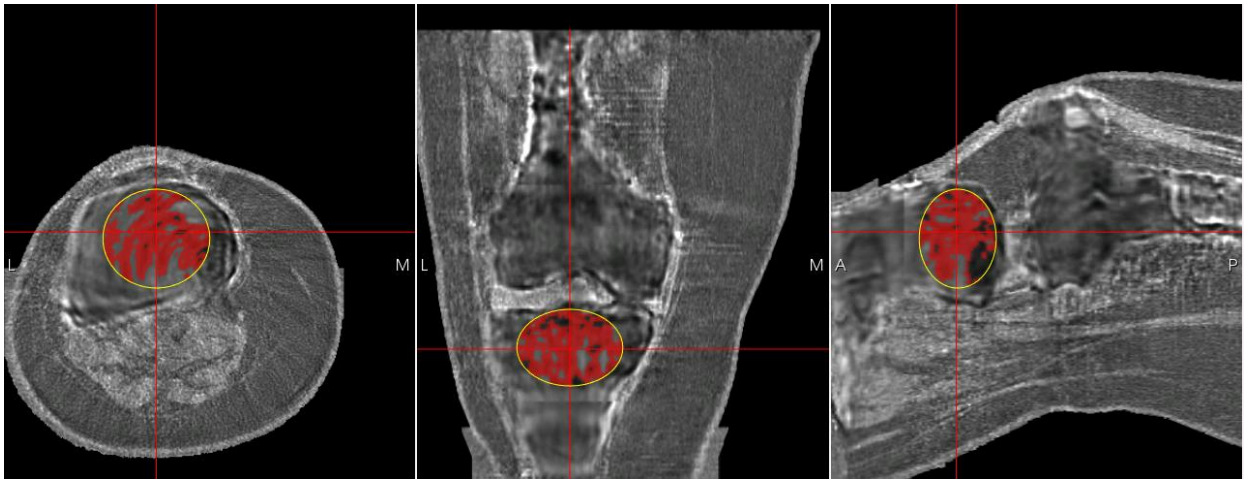

Figure 4: Segmentation of marrow in tibia based on the SOS and constrained by ellipsoid gives average value 1402.2 m/s

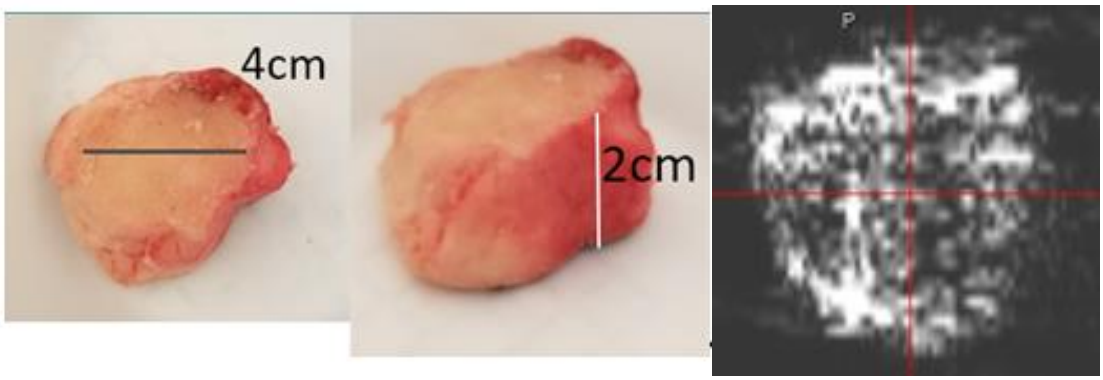

Figure 5: Bovine tibia sample is scanned in the water bath scanner – attenuation image on right showing trabecular nature explicitly.

Attenuation:

The standard tissue model used for attenuation variance with frequency is [22]

$$\alpha(\omega) = \alpha_o \omega^a \quad , \quad \omega = 2\pi f$$

Which leads to the linear relationship:

$$\log \alpha(x, \omega) = \log \alpha_o(x) + a \log \omega$$

The image below shows log-log plot of attenuation vs freq for UCSD-901=071-L – this was a cancer lesion as verified by independent Radiologists.

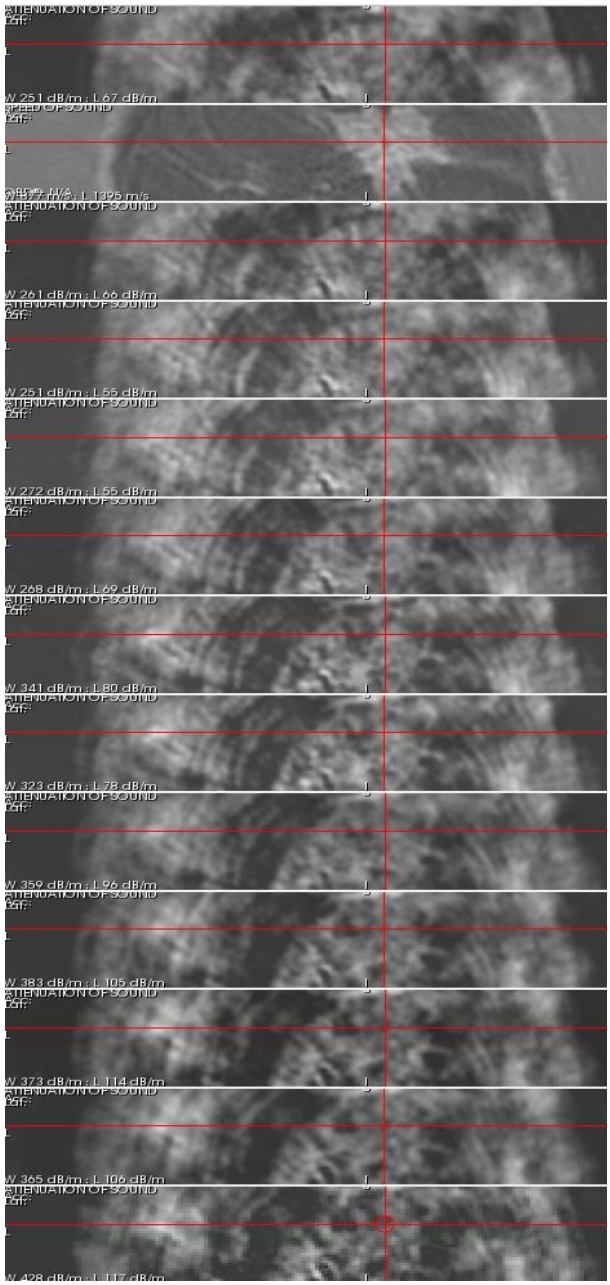

Figure 6: top to bottom: atten at 1.3 MHz, speed of sound image at 1.3 MHz. Subsequent panels show attenuation images at sequentially lower frequencies to .400 MHz. This is a voxel in cancer.

This result is for breast, but similar results hold for tissue (soft) in the knee.

The results below show a power relationship between attenuation and frequency for cancer tissue. This relationship is typical of human tissue. Human tissue follows a power law for attenuation variance with frequency.

Using formula: $\log \alpha(x,\omega) = \log \alpha_o(x) + a \log \omega$, the power law here is a=6.17. The power is different from the standard tissue where: *1<a<2 due* to units used, and our attenuation, which is *really* α/f.

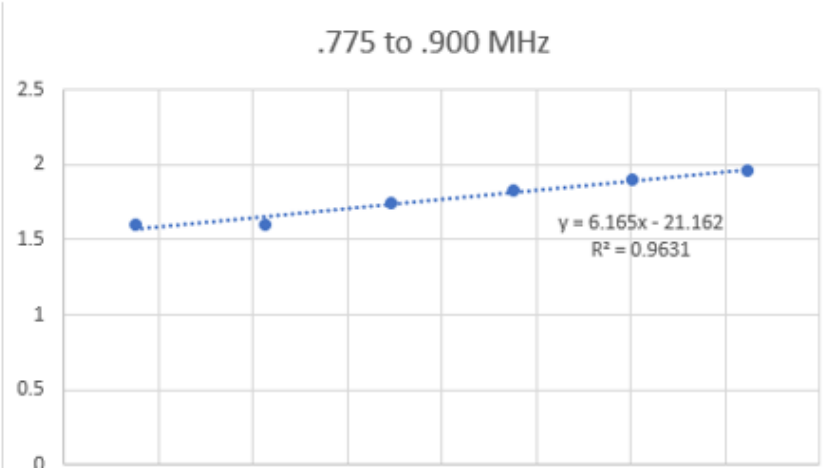

Figure 7: log-log plot of attenuation vs freq (.775, .8, .825, .85, .875, .9, the ROI (region of inspection) is 2 mm diameter centered in the known cancer lesion as determined by the speed of sound map. The speed of sound and the attenuation images are perfectly correlated.

This power law dependence can be used to characterize tissue and may be useful for estimating mass density independently.

Data redundancy: Vology graphy

One of the characteristics of using the 3D model for forward and inverse modelling is that multiple levels of data will thus contribute to a single level of the image. This is quite different from MRI, or when 2D models of wave propagation are used to model wave propagation in ultrasound tomography. (UT).

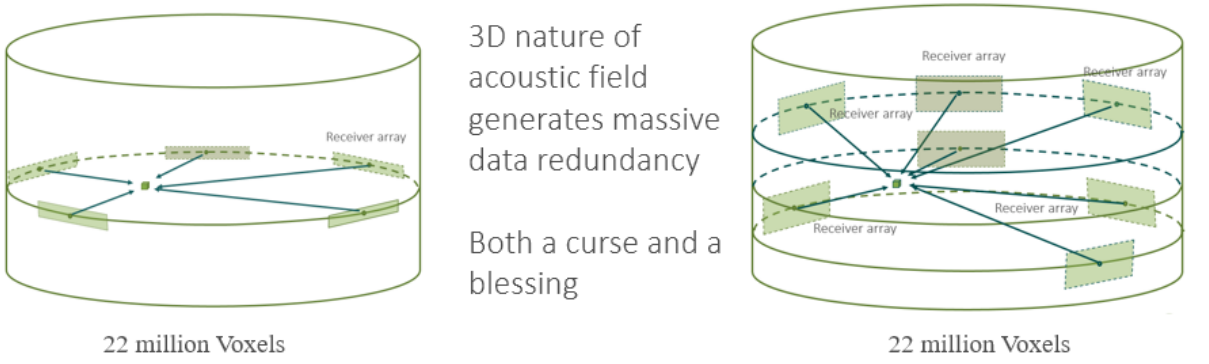

Figure 8: Left the data affecting one voxel for MRI or CT; Right: data affecting one voxel with 3D vology graphy is 200,000 times larger than the data affecting one voxel in 2D algorithms such as CT, MRI or 2D ultrasound tomography. Vology graphy is 3D UT with a 3D model for wave propagation.

The actual redundancy is determined by the height of the acoustic field. An estimated height of ~60 mm indicates approximately 200,000 more data are relevant in the reconstruction of one voxel than if a 2D wave model is used. For this reason, the term volography is used to clarify that 3D wave propagation models are used in the 3D UT reconstruction. That is the reconstruction is not level by level, rather a 'volume' of data contributes to a 'volume' of the image simultaneously.

Verification of tissue values:

The segmentation is carried out for cartilage, ligaments, tendons, fat, skin and muscle tissue and is seen to be within (on average) 1.07%.of the literature values. These values give confidence in the quantitative accuracy of the method, but the values interior to bone appear to be smaller than literature values.

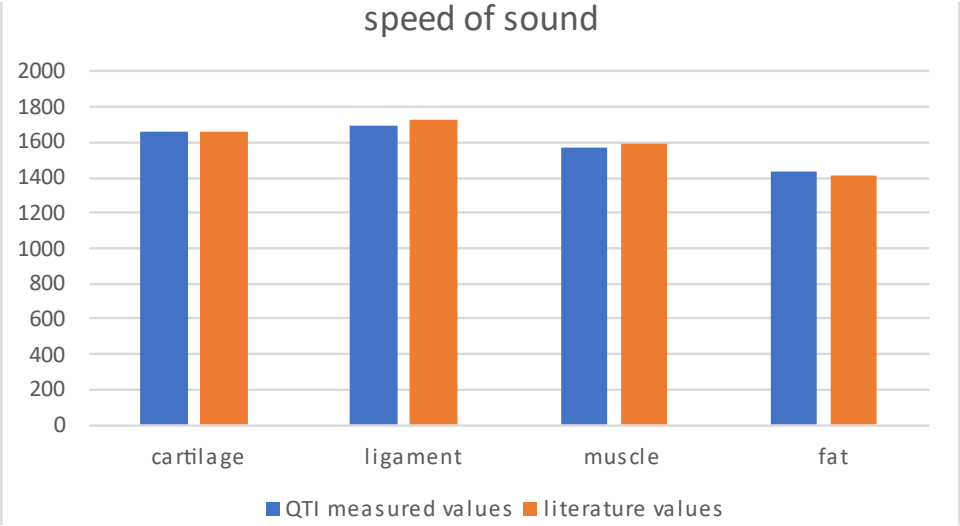

Figure 9: Speed of sound from QTUS images compared with literature values.

Topological considerations:

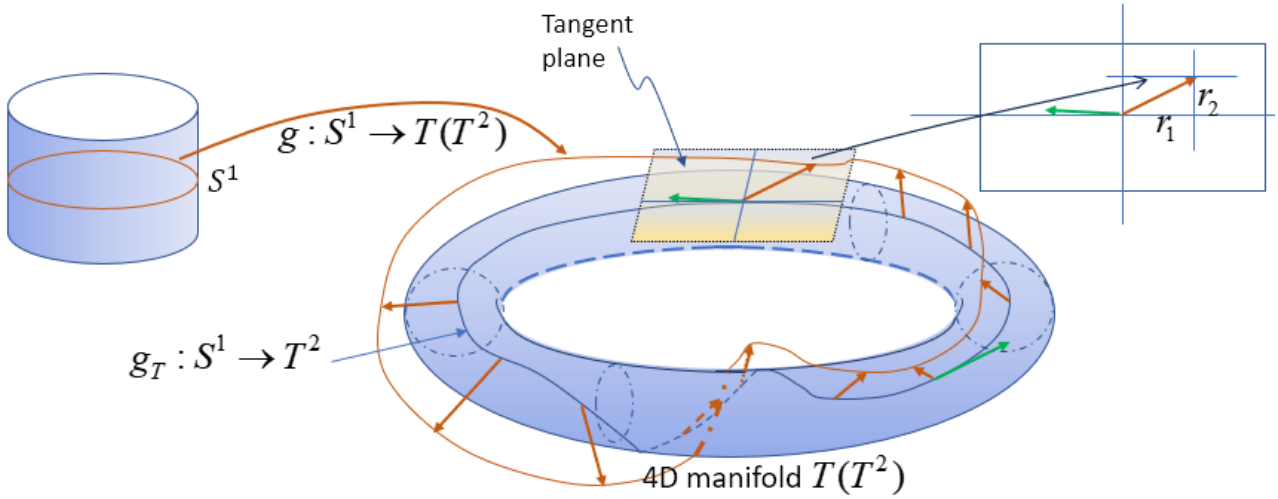

Figure 10: Showing the identification of the plane with the tangent plane at a particular point on the torus. This is generalized to N dimensions easily and shows that the mapping to the red curve is indeed a map to the tangent bundle of the N-torus.

The map $(\theta, l) \in S^1 \times R$ from the position of the array to the data space is signified by

$$\theta \in S^1 \to \left(\theta_1,\cdots,\theta_N,r_1,\cdots,r_N\right) \in T^N \times R^N \approx T(T^N)$$

As discussed above. The key is the identification of $\left(r_1,\cdots,r_N\right) \in R^N$ as (isomorphic to) $\approx T_\Theta\left(T^N\right)$, the tangent bundle at $\Theta \equiv \left(\theta_1,\cdots,\theta_N\right) \in T^N$ the N-torus. This is diagrammed above and since the homotopically equivalent maps $g: S^1 \to T\left(T^N\right)$ form, by definition, the first homotopy group of the tangent bundle to the N-torus. $\pi_1\left(T\left(T^N\right)\right)$, and since any path in the trivial bundle is homotopic to a curve on the torus, , $g_T: S^1 \to T^N$, it is in fact the first homotopy group of the N-torus itself: $\pi_1\left(T^N\right)$, which is known to be isomorphic to: $\pi_1\left(T^N\right) \approx Z \otimes \cdots Z \otimes Z$ [14]. Thus, a typical element is of the form $\mathbf{N} \equiv \left(n_1,\cdots,n_N\right) \in \pi_1\left(T^N\right)$. These give a discrete enumeration of the relevant data for 3D UT.

This analysis shows that as one progresses up the cylinder, representing higher levels of data acquisition in the waterbath, the mappings may change discontinuously represented by a change in the integers making up the elements of the homotopy group: $\mathbf{N} \equiv \left(n_1,\cdots,n_N\right) \in \pi_1\left(T^N\right)$, $n_j \to n_j \pm k_j$ for any *j that changes, and* k_j represents the magnitude of the change. *Note,* that to allow for correct phase unwrapping the distance between the data levels is constrained by $k_j = \pm 1$.

Furthermore, if the vertical height of the cylinder in Figure 12 is frequency, the frequency jumps must also be constrained to only allow the integers to change by unity, to allow correct phase unwrapping.

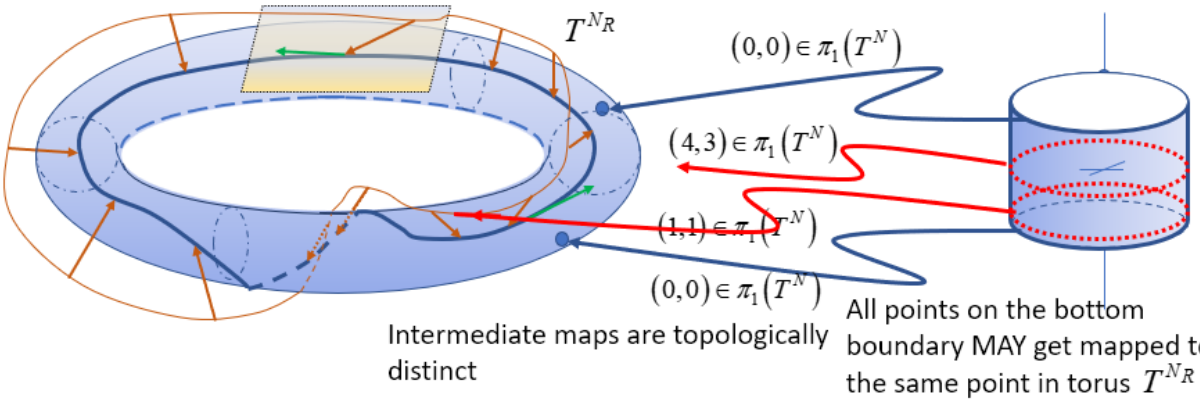

Figure 11: The consideration of multiple maps as the data level progress upwards shows that since each is an element of the first homotopy group, the homotopically distinct maps can change by arbitrary integers if the distance between the levels is too large. Similarly, if the vertical height is interpreted as different frequencies, the frequencies must also be close enough to allow the integers to change by only unity, no more.

Note in Figure 11 that if the top and bottom circles are mapped to distinct single points, the cylinder can be identified as the sphere, S^2. Thus, the second homotopy group of the N-torus is relevant as well under circumstances where the scanned object is small enough.

The tomographic data is shown to be directly related to the first and second homotopy groups of the N-Torus where N is the number of receivers in the array (2048 in our case). This analysis is related to the phase wrapping problem and is ameliorated by the use of multiple columns in the fully 2D receiver array, i.e. 3D redundancy.

Conclusions and Discussion

We show the importance of data redundancy quantitatively and give a unique analysis of the Biot wave data in a tomographic setting that utilizes appropriate tools from algebraic topology and evidence is presented that the Biot wave can be successfully inverted with suitably redundant data.

There is literature evidence that the Biot slow P wave is measured and there is evidence here that this wave can be used to reconstruct estimates related to porosity.

Also a quantitative assessment of relative data redundancy is given for 2D vs 3D algorithms, showing the importance of utilizing full 3D models in 3D UT (i.e. volography).

We show further evidence for the slow Biot wave being used in the reconstruction of the internal bone values and correct marrow SOS values and indicate there is approximately 200,000 times more data contributing to a single voxel in the 3D reconstruction vs the 2D reconstruction. This massive redundancy results in quantitatively accurate reconstruction of ligaments, cartilage, muscle, tendons, etc. and perhaps reconstruction of bone values commensurate with Biot slow waves.

The determination of the frequency dependence of the measured wave numbers at multiple frequencies is carried out and shown to obey a power law, as in other studies.[23]

The fact that these values are close to the literature values for marrow and the slow Biot wave are supportive but not conclusive at this time. A full inversion of the equations in (1) would give further justification that we are seeing a true slow Biot wave.

Acknowledgments

The authors acknowledge the contributions of the QT Imaging team, and in particular Veenda Theendakara for the procurement of the tibia (bovine). The knee images are distinct from but related to the nature paper[24] and [3].

References

[1] J. W. Wiskin, D. T. Borup, E. Iuanow, J. Klock, and M. W. Lenox, "3-D Nonlinear Acoustic Inverse Scattering: Algorithm and Quantitative Results," *IEEE Transactions on Ultrasonics, Ferroelectrics, and Frequency Control,* vol. 64, pp. 1161-1174, 2017.

[2] J. Wiskin, D. Borup, E. Iuanow, J. Klock, and M. Lenox, "Quantitative three dimensional nonlinear inverse scattering and reflection breast imaging: Initial clinical results," *The Journal of the Acoustical Society of America,* vol. 135, pp. 2155-2155, 2014.

[3] J. Wiskin, B. Malik, and J. Klock, "Low frequency 3D transmission ultrasound tomography: technical details and clinical implications," *Zeitschrift für Medizinische Physik,* 2023/06/07/ 2023.

[4] J. Wiskin, B. Malik, C. Ruoff, N. Pirshafiey, M. Lenox, and J. Klock, "Whole-Body Imaging Using Low Frequency Transmission Ultrasound," *Academic Radiology,* vol. 30, pp. 2674-2685, 2023.

[5] J. Wiskin, J. Enders, I. Turkbey, M. Rothberg, M. Merino, S. Xu*, et al.*, *Imaging of prostate cancer with 3D ultrasound tomography* vol. PC12038: SPIE, 2022.

[6] J. W. Enders, C.; Rothberg, M.; Blake, Z.; Noun, J.; Wu, Y.; Wiskin, J.; Daneshvar, M.; Seifabadi, R.; Negussie, A.; Choyke, P.; Boctor, E.; Klock, J.; Toubaji, A.; Merino, M; Turkbey, B.; Wood, B.; Pinto, P.;, "Ultrasound Tomography for Prostate Cancer Imaging: An EX VIVO preliminary study," *EUS proceedings Annual Meeting,* vol. 35, p. 1, Sept. 2022 2022.

[7] C. Williams, M. Daneshvar, Y. Wu, J. Owens-Walton, N. Yerram, P. T. Gomella*, et al.*, "MP22-17 PROSTATE ULTRASOUND TOMOGRAPHY (UT): CORRELATION WITH MRI AND WHOLE MOUNT HISTOPATHOLOGY," *Journal of Urology,* vol. 206, pp. e398-e398, 2021.

[8] W. K. A., "Ultrasonic scattering from cancellous bone: A review," *IEEE Trans. Ultrason. Ferroelectr. Freq. Control,* vol. 55, p. 1432, 2008.

[9] K. Wear, Y. Nagatani, K. Mizuno, and M. Matsukawa, "Fast and slow wave detection in bovine cancellous bone in vitro using bandlimited deconvolution and Prony's method," *J Acoust Soc Am,* vol. 136, pp. 2015-24, Oct 2014.

[10] K. A. Wear, "Mechanisms of Interaction of Ultrasound With Cancellous Bone: A Review," *IEEE Trans Ultrason Ferroelectr Freq Control,* vol. 67, pp. 454-482, Mar 2020.

[11] K. Wear, "Scattering in Cancellous Bone," *Adv Exp Med Biol,* vol. 1364, pp. 163-175, 2022.

[12] H. A. and O. T., "Ultrasonic wave propagation in bovine cancellous bone," *J. Acoust. Soc. Am.,* vol. 101, p. 558, 1997.

[13] W. R. Newman, C. Labuda, and B. K. Hoffmeister, "Spatial variation of ultrasonic attenuation and speed of sound in brain tissue visualized by parametric imaging," *The Journal of the Acoustical Society of America,* vol. 148, pp. 2774-2774, 2020.

[14] R. Bott and L. W. Tu, *Differential Forms in Algebraic Topology*: Springer New York, 2013.

[15] R. Ayala, R. A. Gómez, E. Dominguez, E. D. Murillo, A. Quintero, and A. Q. Toscano, *Algebraic Topology: An Introduction*: Alpha Science International, 2012.

[16] T. J. Haire and C. M. Langton, "Biot theory: a review of its application to ultrasound propagation through cancellous bone," *Bone,* vol. 24, pp. 291-295, 1999/04/01/ 1999.

[17] M. Pakula, "On the modeling of wave propagation in cancellous bone," in *2015 6th European Symposium on Ultrasonic Characterization of Bone*, 2015, pp. 1-4.

[18] F. Mézière, M. Muller, E. Bossy, and A. Derode, "Measurements of ultrasound velocity and attenuation in numerical anisotropic porous media compared to Biot's and multiple scattering models," *Ultrasonics,* vol. 54, pp. 1146-54, Jul 2014.

[19] Z. E. a. Fellah, N. Sebaa, M. Fellah, F. G. Mitri, E. Ogam, W. Lauriks*, et al.*, "Application of the Biot model to ultrasound in bone: Direct problem," *IEEE Transactions on Ultrasonics, Ferroelectrics, and Frequency Control,* vol. 55, pp. 1508-1515, 2008.

[20] F. Z. E. A., C. J. Y., B. S., L. W., and D. C., "Ultrasonic wave propagation in human cancellous bone: Application of Biot theory," *J. Acoust. Soc. Am.,* vol. 116, p. 61, 2004.

[21] A. Hosokawa and T. Otani, "Ultrasonic wave propagation in bovine cancellous bone," *J Acoust Soc Am,* vol. 101, pp. 558-62, Jan 1997.

[22] F. M. Hooi, O. Kripfgans, and P. L. Carson, "Acoustic attenuation imaging of tissue bulk properties with a priori information," *The Journal of the Acoustical Society of America,* vol. 140, pp. 2113-2122, 2016.

[23] J.-W. Jeong, D. C. Shin, S.-H. Do, C. Blanco, N. E. Klipfel, D. R. Holmes*, et al.*, "Differentiation of Cancerous Lesions in Excised Human Breast Specimens Using Multiband Attenuation Profiles From Ultrasonic Transmission Tomography," *Journal of Ultrasound in Medicine,* vol. 27, pp. 435-451, 2008.

[24] J. Wiskin, B. Malik, D. Borup, N. Pirshafiey, and J. Klock, "Full wave 3D inverse scattering transmission ultrasound tomography in the presence of high contrast," *Scientific Reports,* vol. 10, p. 20166, 2020.